IEEE Robotics and Automation Letters (RA-L) paper, presented at ICRA 2026, Vienna, Austria. Cite as RA-L paper.

3D Targeting of a Magnetic Particle in Blood Vessels Using a Field-Free Point in an Open-Type Electromagnetic Actuation System

Seungun Yang, Kim Tien Nguyen, Hyunwoo Kee, Hyoryong Lee, Jayoung Kim, Sukho Park*, *Member, IEEE*

***Abstract*— Recent research has increasingly focused on delivering drug-carrying magnetic particles to diseased areas using electromagnetic actuation (EMA) systems. Particularly, in these systems, creating a field-free point (FFP) and using it to steer magnetic particles in the desired direction has attracted significant attention. However, most previous studies use closed-type EMA systems, which, due to their structural characteristics, are difficult to integrate into actual surgical environments and to operate in conjunction with external imaging systems like X-ray. This study addresses these limitations by using an open-type EMA system, which is better suited for surgical integration. However, an open-type EMA system faces issues such as a significant decrease in magnetic force and an anisotropic magnetic field as the distance from the coils increases in the region of interest (ROI). To overcome these challenges, we optimized the open-type EMA system and proposed a suitable FFP generation method. Furthermore, we presented a targeting algorithm for steering a magnetic particle in blood vessels using anisotropic FFP. This proposed open-type EMA system and the control strategy using FFP were validated through multiphysics simulations and phantom experiments, proving the viability of magnetic particle targeting.**

***Index Terms*—Targeted drug delivery, open-type EMA system, field-free point, magnetic navigation, 3D blood vessel**

I. Introduction

Targeted drug delivery has emerged as a crucial field in medical research and treatment, aiming to enhance therapeutic efficiency while minimizing side effects by selective delivery of drugs to specific areas within the body [1]-[3]. Various drug-loaded particle targeting technologies have been studied, including the use of ultrasound, microbes, light, and magnetic fields [4]. Drug delivery methods using ultrasound, microorganisms, and light each have advantages such as non-invasiveness and high targeting accuracy but are limited by drawbacks like tissue damage, immune responses, and restricted accessibility to deep regions within the body [5]-[9].

Magnetic field-based drug delivery is recognized as one of the most efficient methods for targeting drug-loaded particles, offering precise and non-invasive control of particle positioning using magnetic fields and magnetically loaded particles [10]-[12]. Among these methods, the field-free point (FFP) in electromagnetic actuation (EMA) systems has been widely studied for its ability to generate repulsive forces on magnetic particles surrounding it, steering them to desired locations while minimizing magnetic field gradient decay [13]-[15]. For instance, Y. Kim et al. proposed an FFP navigation system using magnetic potential fields (MPF), enabling stable micro-robot targeting even in dynamic environments [16]. Similarly, C. Kim et al. designed a portable EMA system with minimized size and coil count, suitable for large workspaces [17]. However, closed-type EMA systems in previous studies are impractical for surgical use due to limited access to surgical areas and difficulties in integrating with imaging systems like X-rays.

To overcome these limitations, this study introduces an open-type EMA system. As shown in Fig. 1(a), the open-type system allows sufficient space for surgical operations and facilitates the placement of imaging systems without physical interference, enabling simultaneous EMA operation and imaging. However, the Biot-Savart law reduces magnetic field strength as the distance between the coils and the region of interest (ROI) increases, and the one-sided coil arrangement in open systems causes FFP distortion.

This study addresses these challenges by optimizing the open-type EMA system through improved coil designs, placement adjustments, and a novel FFP generation method (Fig. 1(b)). Specifically, coil optimization compared the traditional ferromagnetic core-based electromagnetic actuator (FEMA) with the composite electro-permanent magnetic actuator (CEPMA), which combines hard and soft magnets with ferromagnetic cores. CEPMA, which demonstrated higher magnetic field strength and gradients, was selected [18]. A six-coil system was optimized for the small animal model. To counteract the inherent weaknesses of open-type systems, a new FFP generation method was developed. As shown in Fig. 1(a), a magnetic particle is injected at a controlled flow rate after using a balloon catheter to block blood flow. The position of the magnetic particle and the geometry of the blood vessel are analyzed to determine the optimal FFP location for effectively steering the magnetic

Manuscript received: April 8, 2025; Revised: June 17, 2025; Accepted: July 21, 2025

This paper was recommended for publication by Editor Jessica Burgner-Kahrs upon evaluation of the Associate Editor and Reviewers' comments.

This work was supported by the Korea Health Technology Development R&D Project through the Korea Health Industry Development Institute (KHIDI), funded by the Ministry of Health & Welfare, Republic of Korea (grant number: HI19C0642).

Seungun Yang, Hyunwoo Kee, Hyoryong Lee and Sukho Park are with the MBR Laboratory, DGIST Daegu 42988, Republic of Korea (e-mail: dysu1236@dgist.ac.kr, mequee@dgist.ac.kr, hr_lee@dgist.ac.kr, shpark12@dgist.ac.kr).

Kim Tien Nguyen. Korea Institute of Medical Microrobotics, Gwangju, 61011, Republic of Korea (e-mail: nkt@kimiro.re.kr).

Jayoung Kim. Department of Biosystems Engineering, Chungbuk National University (CBNU), Chungbuk, 28644, Republic of Korea (e-mail: jaya@cbnu.ac.kr). This article has supplementary material provided by the authors.

Digital Object Identifier (DOI): see top of this page.

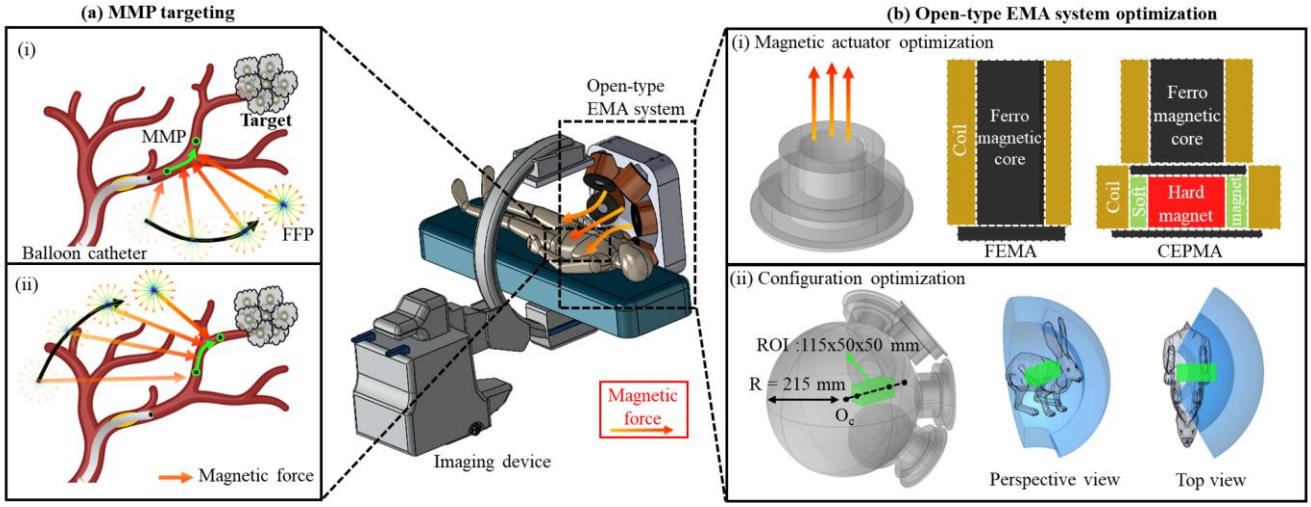

Fig. 1. (a) Schematic diagram of magnetic particle targeting and (b) Schematic of the optimization process for the open-type EMA system.

particle toward the target site.

This paper is structured as follows: In Section 2, we proceed with coil optimization and coil configuration optimization. Section 3 introduces an improved FFP generation method to reduce the distortion of the FFP and obtain a strong magnetic field gradient, and an algorithm to steer a magnetic particle to a desired target. Section 4 validates the proposed open-type EMA system, the improved FFP generation method, and the magnetic particle targeting algorithm through 2D & 3D Y-shaped phantom experiments and a 3D phantom simulating actual liver vasculature. Section 5 presents the discussion, and Section 6 concludes the paper.

II. Open-type EMA System for Magnetic Particle Targeting

A. Electromagnetic actuator optimization

Electromagnetic actuator optimization was conducted using two actuator structures: FEMA and the CEPMA (Fig. 2(a)). The CEPMA structure enhances the magnetic field and gradient by utilizing hard and soft magnets, where the magnetization direction of the soft magnet can either amplify or cancel the magnetic field. Both structures use SS400 as the ferromagnetic core material and enamel-coated copper wire for the coils. The hard and soft magnets in the CEPMA structure are NdFeB N45 and AlNiCo 5, respectively.

The optimization process was performed in the COMSOL optimization module using the Nelder–Mead method, where the objective function was the magnetic field gradient at 115 mm from the coil tip within the ROI of the EMA system [19]. FEMA optimization involved determining design variables, such as core and disk dimensions, as well as the number of coil turns. For CEPMA, additional parameters, including the height of the hard and soft magnets, were optimized. In the EMA system, the mass of each coil was limited to 10 kg, the resistance to 5 Ω, and the maximum current applied to each coil was limited to 20 A. The optimization results showed that CEPMA generated a 50.19% higher magnetic field (27.4 mT) and a 43.0% higher magnetic field gradient (0.466 T/m) compared to FEMA (Table I). Based on this performance advantage, CEPMA was selected for the study, and the coils were fabricated using optimized parameters.

TABLE I Optimized Parameters of Coils

Model Name	l_{core} (mm)	l_{mag} (mm)	r_{core} (mm)	r_{disk} (mm)	l_{disk} (mm)	N_1	N_2	$\left\|\frac{\partial B_z}{\partial z}\right\|$ (T/m)	$\|B_z\|$ (mT)
FEMA	150.5	-	28.6	55.0	15.0	1402	-	0.326	18.2
CEPMA	51.4	23.0	38.6	60.5	5.7	433	261	0.466	27.4

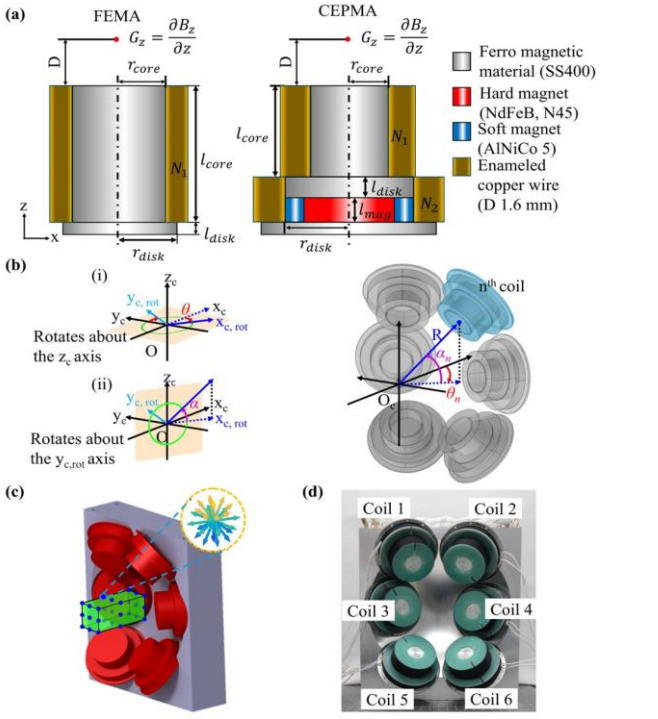

Fig. 2. (a) Structure and geometric parameters of FEMA and CEPMA, (b) Coordinate axis rotation and optimization parameters α_n and θ_n for the configuration optimization of the nth coil, (c) A schematic diagram showing the isotropic factor of the FFP within the ROI, (d) Open-type EMA system fabricated through coil placement optimization.

B. Configuration optimization

In this study, we designed an open-type EMA system for steering magnetic particles within the hepatic blood vessels

of medium-sized animals, specifically New Zealand White rabbits weighing approximately 3 kg. Considering the heart girth of the animal (approximately 37 cm), the ROI was defined to match the size of the liver, with a cuboid of (W)50 x (L)115 x (H)50 mm selected. And the system was designed to generate FFPs at all points within the ROI [20], [21]. While at least four magnetic sources are required for FFP generation, we selected and optimized the configuration of six magnetic coils which can be physically arranged as increasing the number of coils enhances the magnetic force. The coil placement was designed to accommodate operator access and facilitate the top-and-bottom arrangement of X-ray devices, with the system origin (O_c) positioned 215 mm away from the coil tip. Additionally, a 50 mm gap was maintained between the animal and the coils to ensure safety and operational convenience (Fig. 1(b)(ii)).

The configuration optimization is performed in two stages using MATLAB R2022a. First, coil configurations are generated by examining potential interference based on optimized coil geometrical parameters, the distance between O_c and the coil tip, and alignment angles α and θ (Fig. 2(b)). The general idea is to optimize the system configuration to generate isotropic FFP at an arbitrary point inside the ROI, thus inducing a sufficient magnetic force at the targeted point [21].

In the proposed steering strategy used in this work, it is important to have an isotropic FFP generation. Therefore, the isotropic factor of the FFP, δ_{FFP}, which is used as one of the main optimization criteria in this optimization, is defined as the gradient field differences among three basic axes, considering each of the *k* points inside the ROI as follows:

$$\begin{bmatrix} \hat{G}_x \\ \hat{G}_y \\ \hat{G}_z \end{bmatrix} = \begin{bmatrix} \sum_{j=1}^{n} \frac{\partial B_{jx}+\partial B_{jy}+\partial B_{jz}}{\partial x} \\ \sum_{j=1}^{n} \frac{\partial B_{jx}+\partial B_{jy}+\partial B_{jz}}{\partial y} \\ \sum_{j=1}^{n} \frac{\partial \mathrm{B_{jx}}+\partial B_{jy}+\partial B_{jz}}{\partial z} \end{bmatrix} = \hat{G}_x \begin{bmatrix} 1 \\ \hat{G}_y/\hat{G}_x \\ \hat{G}_z/\hat{G}_x \end{bmatrix} \quad (1)$$

$$\delta_{FFP} = \left\| \begin{vmatrix} 1 \\ \hat{G}_y/\hat{G}_x \\ \hat{G}_z/\hat{G}_x \end{vmatrix} - \begin{vmatrix} 1 \\ 1 \\ 1 \end{vmatrix} \right\| \quad (2)$$

Here, B_{jx}, B_{jz}, B_{jz} and $\frac{\partial B_{jx}}{\partial x}$, $\frac{\partial B_{jx}}{\partial y}$, $\frac{\partial B_{jx}}{\partial z}$ are the x, y, and z terms of unit-current magnetic field and gradient field values at a point $\boldsymbol{p}(x, y, z)$ generated by j^{th} coil , respectively. And $\hat{G}_x$, $\hat{G}_y$, and $\hat{G}_z$ are the *x*, *y*, and *z* terms of the resultant gradient field at point $\boldsymbol{p}$ generated by *n* number of magnetic sources.

As shown in Fig. 2(c), δ_{FFP} was calculated for *k* (*k* = 144) equally distributed points inside the ROI of a certain coil configuration. Among 1000 candidate configurations, an optimization process was performed to determine the best configuration. The configuration that creates the most isotropic FFP corresponds to the one with the smallest δ_{FFP} among all coil configurations. The angles of each optimized coil resulting from this process are listed in Table II, and the fabricated open-type EMA system can be seen in Figure 2(d).

TABLE II OPTIMIZED COIL CONFIGURATION PARAMETERS

Coil numbers		1	2	3	4	5	6
Placement	θ (°)	-27	25	-31.8	28.9	-25	28.6
	α (°)	39.5	38	1.7	-1.7	-39.5	-40.1

III. MAGNETIC PARTICLE TARGETING STRATEGY

A. Analytic model

A dynamic model based on Newtonian mechanics was developed to describe magnetic particle targeting. The governing equation presented below is based on well-established formulations in magnetic microcarrier dynamics [21], [22], [23].

$$m_p \frac{d\boldsymbol{v}_p}{dt} = \boldsymbol{F}_{mag} + \boldsymbol{F}_{drag} + \boldsymbol{F}_g + \boldsymbol{F}_{etc} \quad (3)$$

where, m_p and $\boldsymbol{v}_p$ represent the mass and velocity of the magnetic particle. The terms $\boldsymbol{F}_{mag}$, $\boldsymbol{F}_{drag}$, and $\boldsymbol{F}_g$ correspond to the magnetic force, drag force, and gravitational force acting
on the particle. The term $\boldsymbol{F}_{etc}$ accounts for the remaining forces, such as electrostatic, adhesion, which are considered negligible.

The magnetic force is given by:

$$\boldsymbol{F}_{mag} = \mu_0 V_p \boldsymbol{M}(\boldsymbol{H}) \nabla \boldsymbol{H} \quad (4)$$

where μ_0 is the permeability of free space, V_p is the volume of the magnetic particle, $\boldsymbol{M}(\boldsymbol{H})$ is the magnetization of the particle due to the external magnetic field, and $\nabla \boldsymbol{H}$ is the magnetic field gradient.

The drag force follows Stokes' law:

$$\boldsymbol{F}_{drag} = 6\pi\eta r(\boldsymbol{v}_f - \boldsymbol{v}_p) \quad (5)$$

where η is the viscosity of fluid, r is the radius of the magnetic particle, and $\boldsymbol{v}_f$ is the fluid velocity. Given that the Reynolds number in the experiments does not exceed 1, the system is governed by Stokes' law.

B. FFP generation method

The targeting algorithm generates an operational plane ($x'y'$) at each time step. The position of the particle at each time step (q_k) is the origin of the plane, and the desired force vector (F_k) aligns with the x' axis, while the plane's normal vector aligns with z'.

In previous studies, the following equations were used for the FFP generation [17], [21].

$$\begin{bmatrix} \widehat{\boldsymbol{B}}_{x'}(\boldsymbol{p}) \\ \widehat{\boldsymbol{B}}_{y'}(\boldsymbol{p}) \\ \widehat{\boldsymbol{B}}_{z'}(\boldsymbol{p}) \\ \widehat{\boldsymbol{G}}_{x'}(\boldsymbol{p}) \\ \widehat{\boldsymbol{G}}_{y'}(\boldsymbol{p}) \\ \widehat{\boldsymbol{G}}_{z'}(\boldsymbol{p}) \end{bmatrix} \begin{bmatrix} i_1 \\ i_2 \\ \vdots \\ i_n \end{bmatrix} = \begin{bmatrix} B_{x'}(\boldsymbol{p}) \\ B_{y'}(\boldsymbol{p}) \\ B_{y'}(\boldsymbol{p}) \\ G_{x'}(\boldsymbol{p}) \\ G_{y'}(\boldsymbol{p}) \\ G_{z'}(\boldsymbol{p}) \end{bmatrix} = \begin{bmatrix} \boldsymbol{0}_{3\times1} \\ \boldsymbol{G}_{desired_{3\times1}} \end{bmatrix} \quad (6)$$

$$\boldsymbol{A}(\boldsymbol{p})\boldsymbol{i} = \boldsymbol{b}_{desired} \leftrightarrow \boldsymbol{i} = \boldsymbol{A}^{+}(\boldsymbol{p})\boldsymbol{b}_{desired} \quad (7)$$

where $\widehat{\boldsymbol{B}}_{x'}(\boldsymbol{p}), \widehat{\boldsymbol{B}}_{y'}(\boldsymbol{p}), \widehat{\boldsymbol{B}}_{z'}(\boldsymbol{p}), \widehat{\boldsymbol{G}}_{x'}(\boldsymbol{p}), \widehat{\boldsymbol{G}}_{y'}(\boldsymbol{p})$, and $\widehat{\boldsymbol{G}}_{z'}(\boldsymbol{p})$ represent the unit-current magnetic field and gradient field vectors (1×n) in the x', y', and z' directions at point $\boldsymbol{p}$, generated by unit current in each coil. And $B_{x'}(\boldsymbol{p}), B_{y'}(\boldsymbol{p}), B_{z'}(\boldsymbol{p})$, $G_{x'}(\boldsymbol{p}), G_{y'}(\boldsymbol{p})$, and $G_{z'}(\boldsymbol{p})$ represent the desired magnetic field and gradient field in the x', y', and z' directions at point $\boldsymbol{p}(x', y', z')$. Therefore, $\boldsymbol{b}_{desired}$ denotes the desired matrix and $\boldsymbol{A}(p)$ denotes the unit matrix corresponding to each coil at point $\boldsymbol{p}$. As shown in (6), the required current for FFP generation is determined by solving the inverse matrix after substituting $B_{x'}(\boldsymbol{p}) = B_{y'}(\boldsymbol{p}) = B_{z'}(\boldsymbol{p}) = 0$ and the desired gradient values. Previous methods enforce $G_{x'}(\boldsymbol{p}) = G_{y'}(\boldsymbol{p}) = G_{z'}(\boldsymbol{p})$, leading to a weaker magnetic gradient and reduced force on the magnetic particle due to anisotropy open-type EMA system.

To overcome this, we propose a new FFP generation method:

$$\begin{bmatrix} \widehat{\boldsymbol{B}}_{x'}(\boldsymbol{p}) \\ \widehat{\boldsymbol{B}}_{y'}(\boldsymbol{p}) \\ \widehat{\boldsymbol{B}}_{z'}(\boldsymbol{p}) \\ \widehat{\boldsymbol{G}}_{x'}(\boldsymbol{p}) \end{bmatrix} \begin{bmatrix} i_1 \\ i_2 \\ \vdots \\ i_n \end{bmatrix} = \begin{bmatrix} B_{x'}(\boldsymbol{p}) \\ B_{y'}(\boldsymbol{p}) \\ B_{z'}(\boldsymbol{p}) \\ G_{x'}(\boldsymbol{p}) \end{bmatrix} = \begin{bmatrix} \boldsymbol{0}_{3\times1} \\ G_{desired_{1\times1}} \end{bmatrix}$$

$$\leftrightarrow \quad \boldsymbol{A}(\boldsymbol{p})\boldsymbol{i} = \boldsymbol{b}_{desired} \tag{8}$$

$$\boldsymbol{i} = argmin\left(\left| \, |G_{x'}(\boldsymbol{p})| - |G_{y'}(\boldsymbol{p})| \, \right| \right)$$
$$s.t. \quad \boldsymbol{A}(\boldsymbol{p})\boldsymbol{i} = \boldsymbol{b}_{desired} \tag{9}$$

Here, $\widehat{\boldsymbol{B}}_{x'}(\boldsymbol{p}), \widehat{\boldsymbol{B}}_{y'}(\boldsymbol{p}), \widehat{\boldsymbol{B}}_{z'}(\boldsymbol{p})$, and $\widehat{\boldsymbol{G}}_{x'}(\boldsymbol{p})$ represent the 1×n matrices of the unit-current magnetic field and gradient in the x'-direction at point $\boldsymbol{p}$. The previous FFP generation method considered gradients along all three axes. However, in the open-type EMA system, the equal gradient condition reduces the FFP strength due to insufficient generation along certain axes. Therefore, in this study, only the gradient term in the main axis (x'-axis), which applies the desired force, is considered. This increases redundancy and allows for larger magnetic field gradients. In accordance with (9), we selected the optimal current combination that minimizes the difference between the gradient terms in the x' and y' directions in the set of combinations that satisfy the predefined conditions, thereby ensuring the isotropy of the FFP.

For intuitive understanding, the xyz coordinate system based on the ROI was used instead of the $x_c y_c z_c$ coordinate system employed in the coil configuration, as shown in Fig. 3(a). Simulations using COMSOL Multiphysics were performed to generate FFPs at specific points on the xy-plane - (10, 0, 0), (57.5, 0, 0), and (105, 0, 0) - with both the previous and proposed methods. Using the proposed method, FFPs displayed higher magnetic field strengths and gradients with improved isotropy in the operational plane, as shown in Fig. 3(b) and (c).

As shown in Fig. 3(d), quantitative comparison of FFPs generated along the main axis (x-axis) and sub axis (y-axis) at 1 mm intervals demonstrated significantly higher magnetic field gradients with the proposed method. At (10, 0, 0), (57.5, 0, 0), and (105, 0, 0), the proposed method produced x-axis gradients of 0.6370, 0.2288, and 0.1111 T/m, compared to 0.1920, 0.0432, and 0.0276 T/m for the previous method. Sub-axis (y-axis) gradients followed a similar result. These results

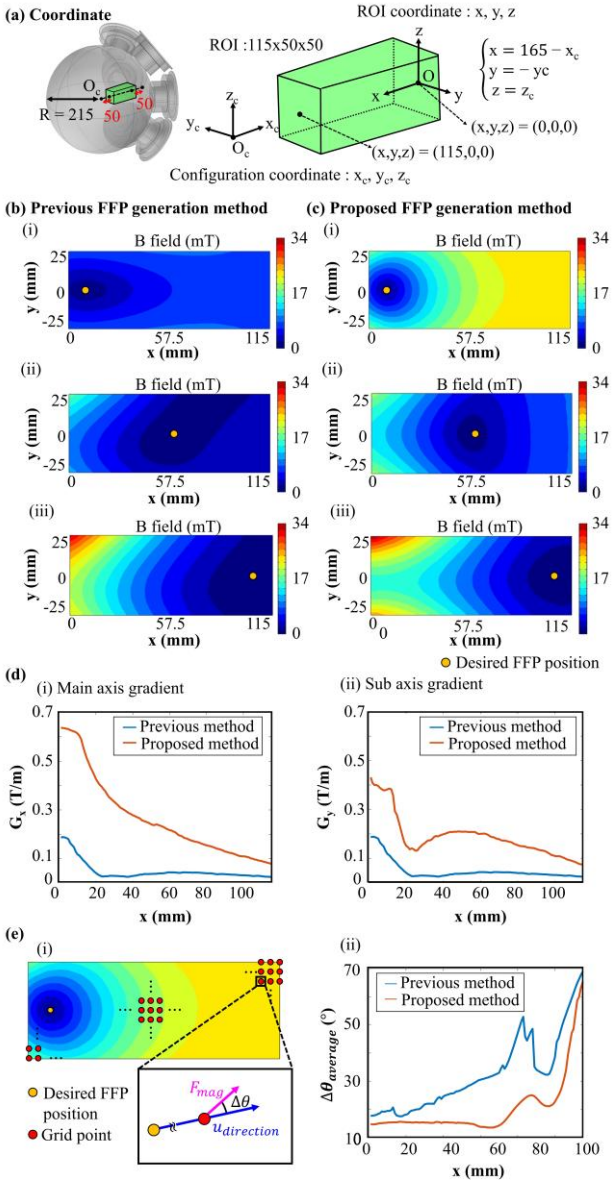

Fig. 3. (a) Relationship and equations defining the coordinates used for placement optimization relative to the ROI, (b) Magnetic field distribution on the xy-plane for FFP generation at (10,0,0), (57.5,0,0), and (105,0,0) using the previous FFP generation method [17], [21], (c) Magnetic field distribution on the xy-plane at the same positions using the proposed FFP generation method, (d) Comparison of magnetic field gradients on FFP center along the main and sub-axis using both FFP generation methods, (e) (i) Schematic diagram showing the calculation of the average angle difference ($\Delta\boldsymbol{\theta}_{average}$), and (ii) $\Delta\boldsymbol{\theta}_{average}$ measured at various distances

confirm that the proposed FFP generation method exhibits substantially higher magnetic fields and gradients than the previous method in the operational plane.

In magnetic steering using FFP, isotropy, alongside the strength of the magnetic field and gradient, is crucial for precise control. An isotropic FFP ensures alignment between the repulsive force (F_{mag}) and the directional vector ($u_{direction}$), enabling accurate targeting. In contrast, reduced isotropy complicates force prediction and increases targeting errors. To evaluate isotropy within the operational plane, a grid of 116 × 51 points spaced at 1 mm intervals was established. At each x-axis point, FFPs were generated, and the angle differences ($\Delta\theta$) between F_{mag} and $u_{direction}$ to

the grid points were measured. The average angle difference ($\Delta\theta_{average}$) served as an isotropy indicator (Fig. 3(e)(i)).

Fig. 3(e)(ii) compares $\Delta\theta_{average}$ for FFPs generated at three specific points: (10, 0, 0), (57.5, 0, 0), and (105, 0, 0). The proposed method produced $\Delta\theta_{average}$ values of 15.22, 13.97, and 31.76 degrees, respectively, outperforming the previous method's 19.53, 29.50, and 52.30 degrees. These results demonstrate the proposed method's enhanced isotropy in the operational plane, addressing open-type EMA limitations by mitigating reductions in magnetic field strength.

C. Magnetic particle targeting algorithm

Tracking the real-time position of the small magnetic particles within blood vessels via imaging poses significant challenges. To address this, we propose an open-loop magnetic particle targeting algorithm. In this approach, we assume a surgical scenario involving a balloon catheter. Initially, the catheter is inserted into the desired blood vessel entrance, and the balloon is inflated to block the blood flow. Subsequently, the magnetic particle is injected through the catheter along with a fluid, allowing the fluid flow to carry the particle. To compensate for the relatively weak magnetic forces generated by the open-type EMA system, the algorithm dynamically determines the location of FFP at each timestep based on the shape of the blood vessel, applying continuous magnetic forces to guide the particle along the desired path.

This study introduces a method that selects operational planes for effective force application, enabling the particle to move toward the desired outlet based on geometric and fluid flow data acquired via COMSOL Multiphysics. The paths from the inlet to the branch points, as well as between consecutive branch points, are divided into segments. Using these segments, a trajectory is established to guide the particle.

As shown in Fig. 4(a), a timeline is generated for each segment between branch points using the targeting algorithm, and these are integrated into a complete timeline (Fig. 4(d)). In the rth segment, based on the acquired fluid flow then created using the central line points, and the optimal FFP location is selected for each operational plane. To ensure the operational plane spans the appropriate force direction for guiding the magnetic particle toward the desired outlet, the first plane is generated at the branch point to account for its geometry. Subsequent operational planes are then generated in reverse order, moving progressively towards the inlet or the previous branch point.

Fig. 4(b) shows the process of generating the operational plane and selecting the FFP location at the branch point q_{m_r}. Initially, as shown in Fig. 4(b)(i), the first plane (plane m_r) is established by passing through the branch point q_{m_r}, and two additional points q_{b1} and q_{b2}, located at differential distances from q_{m_r} along the central lines of the subsequent sections.

Next, as depicted in Fig. 4(b)(ii), to adjust the force direction at the FFP location, multiple candidate FFPs are generated at 1 mm intervals along the operational plane m_r. From these candidates, the FFP that provides the largest force component F_{m_r} in the desired outlet is selected. The force direction guiding the magnetic particle toward the target branch is set perpendicular to the projection vector

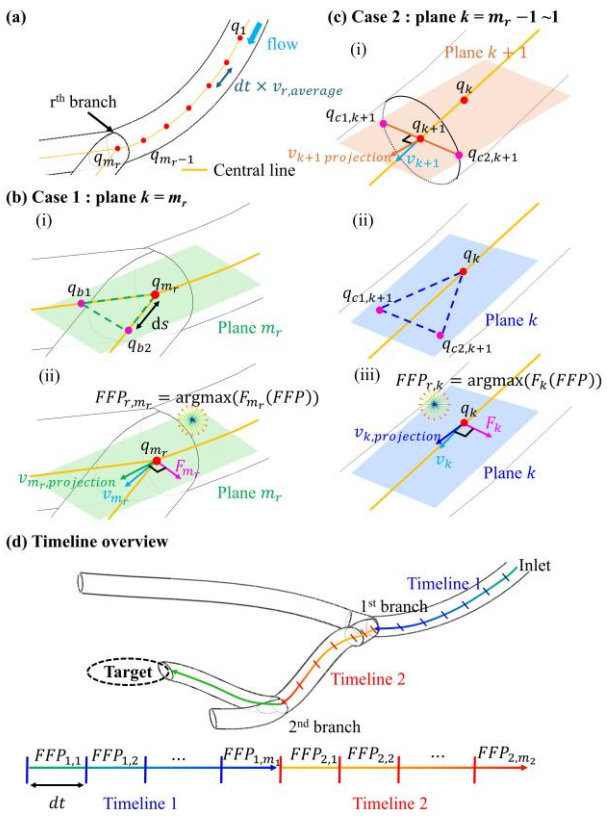

Fig. 4. Overview of the targeting algorithm: (a) Segmentation of flow-based unit time intervals at the rth branch, (b) For plane $k = m_r$: (i) Generation of plane m_r and (ii) Method for selecting FFP_{r,m_r}, (c) For planes $k = m_r$ - 1to 1 : (i) Determination of $q_{c1,k+1}$ and $q_{c2,k+1}$, (ii) Generation of plane k, and (iii) Method for selecting $FFP_{r,k}$, and (d) Overview of the entire timeline, combining the FFP application timelines for each branch.

$v_{m_r,projection}$, which is the velocity vector v_{m_r} at the central point q_{m_r}, projected onto plane m_r. This force direction aligns with one of the two vectors passing through plane m_r towards the desired outlet. To maximize the magnetic field gradient in the direction of the desired force, the selected vector is designed as the main axis (x') during the FFP generation process.

Fig. 4(c) shows the process of generating operational planes and selecting the FFP location at points preceding the branch point (e.g., $q_{m_r-1}, q_{m_r-2}, \cdots, q_k, \cdots, q_1$). For any given point q_k, as depicted in Fig. 4(c)(i) and (ii), the operational plane is created by passing through point q_{k+1} and the contact points $q_{c1,k+1}$ and $q_{c2,k+1}$, where the perpendicular line from the projected vector $v_{k+1,projection}$ (the velocity vector v_{k+1} at the central point q_{k+1}, projected onto the plane m_{k+1}) intersects the blood vessel wall. Subsequently, as shown in Fig. 4(c)(iii), multiple candidate FFPs are generated along the operational plane. The FFP with the largest force component F_k in the direction of the desired outlet is then selected, ensuring optimal guidance of the magnetic particle toward the target.

Dynamic simulations are then conducted to verify whether the magnetic particle moves toward the desired branch along the timeline by applying the magnetic field. If the simulations indicate that the particle fails to move in the desired direction on certain timelines, the input flow rate is reduced to allow an increase of one in the number of FFP locations at points, as

Algorithm 1: Magnetic Particle Targeting Algorithm.

Input: v_{inlet}, dt, channel geometry
Output: FFP Timeline

for r = 1 to N **do**
  central line ← Get_centralline (channel geometry (r))
  roof = 0
  while roof = 0 **do**
    $v_{r,\,average}$ ← Fluid_simul (v_{inlet}, channel geometry)
    $\{q_1 \sim q_{mr}\}$ ← Get_dots (central line, interval = $v_{r,\,average}dt$)
    for k = m_r **do**
      q_{b1}, q_{b2} ← Get_dots (central line, interval = ds)
      plane k ← Get_plane (q_{b1}, q_{b2}, q_k)
      $v_{k,\,projection}$ ← projection (v_k, plane k)
      F_k ← Get_verticalvector ($v_{k,\,projection}$, plane k)
      FFP list ← Get_grid (origin = q_k, main axis = F_k, interval = 1 mm, plane = plane k)
      $FFP_{r,\,k}$ ← argmax (F_k (FFP list))
    end for
    for k = m_r – 1 to 1 **do**
      line k ← Get_verticalline ($v_{k+1,\,projection}$, plane k+1, q_{k+1})
      $q_{c1,\,k+1}$ $q_{c2,\,k+1}$ ← Contact_point (line k, channel geometry)
      plane k ← Get_plane ($q_{c1,\,k+1}$ $q_{c2,\,k+1}$, q_k)
      $v_{k,\,projection}$ ← projection (v_k, plane k)
      F_k ← Get_verticalvector ($v_{k,\,projection}$, plane k)
      FFP list ← Get_grid (origin = q_k, main axis = F_k, interval = 1 mm, plane = plane k)
      $FFP_{r,\,k}$ ← argmax (F_k (FFP list))
    end for
    Goal ← Dynamic_simul ({$FFP_{r,\,1}$, $FFP_{r,\,2}$, … $FFP_{r,\,mr}$})
    if Goal = True **then**
      roof = 1
      Timeline r ← {$FFP_{r,\,1}$, $FFP_{r,\,2}$, …, $FFP_{r,\,mr}$}
    Else
      v_{inlet} ← Length (central line)v_{inlet} / (Length (central line) + $v_{inlet}dt$)
    end if
  end while
end for
return FFP timeline ← {Timeline 1, Timeline 2, …, Timeline N}

described in line 29 of Algorithm 1. It extends the duration that the particle remains under the influence of the magnetic force. This adjustment is repeated across all timelines until the magnetic particle is successfully guided toward the desired branch. Once the optimal movement is achieved, a complete timeline is constructed by sequencing the optimized FFPs according to the movement of the particle. The FFPs are then applied in sequence to guide the particle along the final trajectory. This entire process is described in Algorithm 1.

IV. Experiments

A. Experimental setup

The 2D and 3D Y-shaped phantoms were fabricated using stereolithography (SLA) 3D printing with Clara A material. The 3D blood vessel phantom experiment targeted transcatheter arterial embolization (TACE). The 3D blood vessel phantom was created from a model of real liver vasculature obtained by CT imaging and printed using SLA 3D printing with Accura ClearVue material. The magnetic particles were made from alginate, a biocompatible and biodegradable material, embedded with Fe_3O_4 magnetic nanoparticle. The size of the magnetic particles was designed to be approximately 450–500 μm, within the typical range of embolic particles (40–500 μm), to enhance imaging

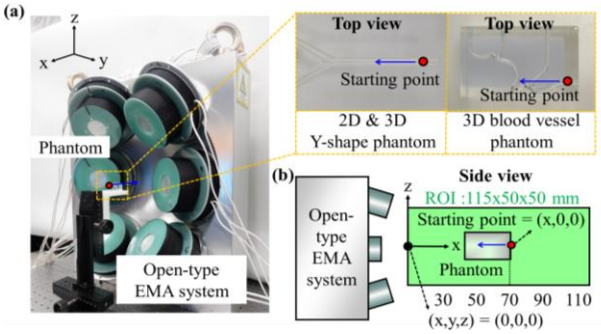

Fig. 5. (a) Open-type EMA system and phantom setup, and (b) Positioning of the phantom relative to the ROI of the open-type EMA system and variation of the starting point.

performance. The particle has a magnetization value of about 24 emu/g, and a density is 1380 kg/m^3. A 60% glycerol solution was used as the fluid because its properties closely resemble those of blood at low flow rates. To enhance visibility, pigment was mixed into the fluid, helping distinguish between the fluid and the phantom walls and aiding observation of the phantom. The experiments were conducted with an input flow rate of 0.65 mL/min for the Y-shaped channels and 0.7 mL/min for the 3D blood vessel channel. Fluid analysis and magnetic field analysis were conducted using COMSOL Multiphysics, and the resulting fluid velocity data were incorporated into MATLAB R2022a for magnetic particle simulations. As shown in Fig. 5(b), five starting points (30, 50, 70, 90, and 110 mm) were used for experiments, with the inlet of the phantom aligned along the x-axis of the system, extending from the outside toward the inside. Each experiment was repeated 50 times, and delivery efficiency was defined as the ratio of successful deliveries to the total trials.

B. Magnetic particle targeting in 2D & 3D Y-shaped phantom

Experiments were conducted on the 2D and 3D Y-shaped phantoms to evaluate the performance of the proposed open-type EMA system, FFP generation method, and magnetic particle targeting algorithm. Initially, magnetic particle targeting was tested on the 2D Y-shaped phantom. As shown in Fig. 6(a), the inlet angle ($\theta_{phantom}$) relative to the x-axis was designed and fabricated to be -45, 0, and 45 degrees. The phantom comprises two key sections: the connecting part, where the Tygon tube attaches to the phantom, and the actuation part, where the magnetic particle is exposed to magnetic forces. The distance from the inlet to the branch is 30 mm, with the actuation part about 25 mm. Video 1 shows the targeting experiments at a starting point of 70 mm. It validates that the magnetic particle was successfully targeted to the desired outlet in the 2D Y-shaped phantom.

Fig. 6(c) summarizes the experimental results of magnetic particle targeting at five starting points in three 2D Y-shaped phantoms. Without magnetic force, particle distribution depended on the inlet angle ($\theta_{phantom}$) : for $\theta_{phantom}$= -45°, 20% of particles reached outlet 1 and 80% outlet 2; for $\theta_{phantom}$= 0°, the distribution was even (50% each); and for $\theta_{phantom}$ = 45°, 82% reached outlet 1 and 18% outlet 2. With the proposed system and algorithm, 100% of particles were guided to the target outlet for starting points of 30–70 mm. At a starting point of 90 mm, an average of 98.3% (with a

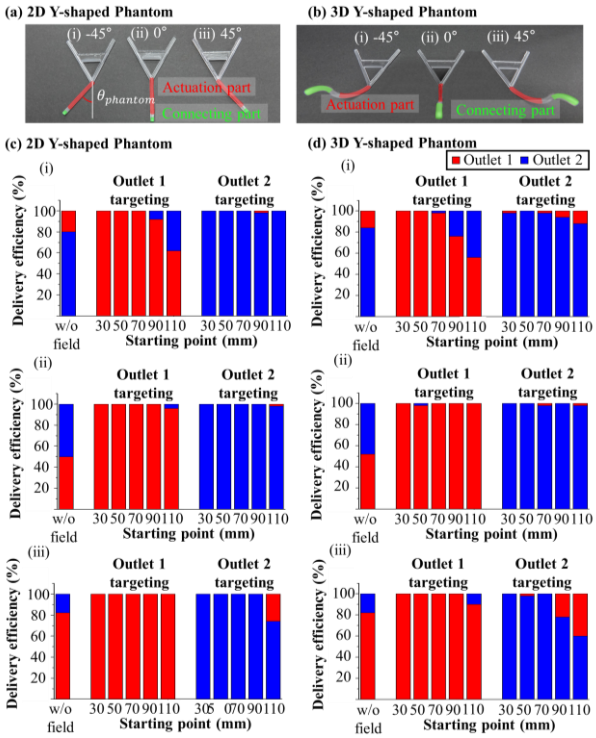

Fig. 6. (a) Fabricated 2D Y-shape phantom, (b) Fabricated 3D Y-shape phantom, (c) Delivery efficiency of magnetic particles towards outlet 1 and 2 from 5 different starting points (30~110 mm) for: (i) 2D -45°, (ii) 2D 0°, and (iii) 2D 45° phantom (n = 50), (d) Delivery efficiency of magnetic particles towards outlet 1 and 2 from 5 different starting points (30~110 mm) for: (i) 3D -45°, (ii) 3D 0°, and (iii) 3D 45° phantom (n = 50).

minimum of 92%) of the particles reached the target outlet. At a starting point of 110 mm, the targeting success rate averaged 88.3%, with a minimum of 62% reaching the desired outlet. As depicted in Fig. 6(b), the 3D Y-shaped phantom relative to the x-axis ($\theta_{phantom}$) was designed and fabricated to be -45, 0, and 45 degrees. To enable a direct comparison with the 2D Y-shaped phantom experiments, the distance from the inlet to the branch was designed as a 20 mm-radius arc. Additionally, 70% of this arc was designed as the actuation part, closely matching the length of the actuation part used in the 2D Y-shaped phantom experiments. Video 2 shows the targeting experiments at a starting point of 70 mm. It validates that the magnetic particle was successfully targeted to the desired outlet in the 3D Y-shaped phantom.

Fig. 6(d) summarizes the experimental results for the magnetic particle targeting at five starting points in three 3D Y-shaped phantoms. Without magnetic force, particle distribution varied by phantom: for $\theta_{phantom}$= -45°, 16% of particles reached outlet 1 and 84% outlet 2; for $\theta_{phantom}$= 0°, 52% reached outlet 1 and 48% outlet 2; and for $\theta_{phantom}$= 45°, 82% reached outlet 1 and 18% outlet 2. With the proposed system and algorithm, an average of 99.3% (minimum of 98%) of particles reached the desired outlet for starting points of 30–70 mm. At a starting point of 90 mm, the average success rate was 91.3% (minimum of 76%), and for a starting point of 110 mm, the average delivery efficiency was 82% (minimum of 56%).

For both the 2D and 3D Y-shaped phantoms, the delivery efficiency decreased beyond the starting point of 70 mm. This is because the magnetic force decreases as the distance

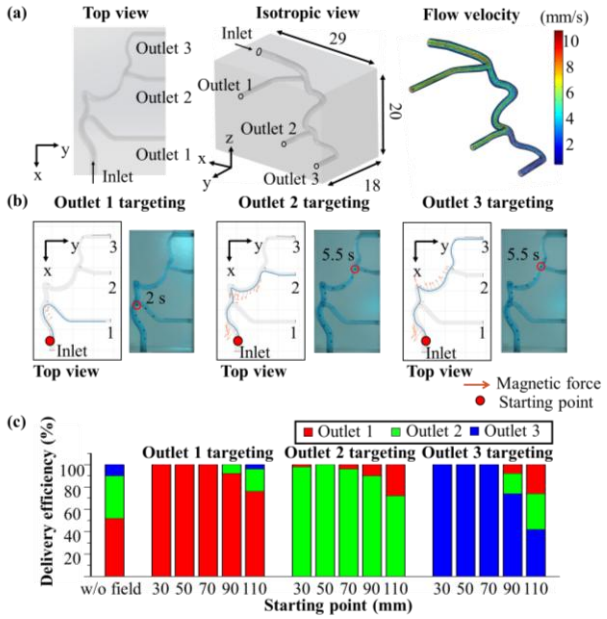

Fig. 7. (a) Geometry of the 3D blood vessel phantom and the fluidic velocity distribution, (b) Simulation and experimental results at the starting point of 70 mm, showing the trajectories and magnetic forces applied to magnetic particles targeting outlet 1, 2, and 3, and (c) Delivery efficiency of magnetic particles directed towards outlet 1, 2, and 3 from 5 different starting points (30~110 mm) in the targeting experiment (n = 50).

between the system and the phantom increases, resulting in an increase in the relative influence of non-magnetic forces acting on the particle. In addition, the 3D Y-shaped phantom exhibited lower delivery efficiency at the same starting points compared to the 2D Y-shaped phantom. This decrease is presumed to be due to the weaker magnetic force with increasing distance between the system and the phantom, despite the same actuation part length.

C. Magnetic particle targeting in 3D blood vessel phantom

Simulations and experiments for magnetic particle targeting were conducted in the 3D blood vessel phantom. Fig. 7(a) shows the geometry of the 3D blood vessel phantom model, and the fluid velocity distribution obtained from simulations. As shown in Fig. 7(a), the 3D blood vessel phantom consists of one inlet, two branches, and three outlets. The inlet has an internal diameter of 1.5 mm, while the outlets have diameters of 1.0 mm, with the channels gradually narrowing from the inlet to the outlets. Fig. 7(b) and Video 3 present the results of simulations and experiments using the proposed targeting algorithm to guide the magnetic particle to the desired outlet from a starting point of 70 mm in the phantom. The figure shows the particle trajectories and magnetic forces applied during the simulation, displayed at 0.2-second intervals, while the experimental results depict the movement of the particle at 0.5-second intervals. Both the simulations and experiments confirm that the magnetic particle is successfully guided to the desired outlets, following similar trajectories in each case.

Fig. 7(c) summarizes the experimental results for targeting the magnetic particle to outlets 1, 2, and 3 from five different starting points in the 3D blood vessel phantom. Without magnetic force, the particles followed the fluid flow, with 52% reaching outlet 1, 38% reaching outlet 2, and 10% reaching outlet 3. When using the proposed open-type EMA system and targeting algorithm, the delivery efficiency to the desired

outlet was at least 90% for starting points of 90 mm or less, and at least 72% for starting points of 110 mm. Specifically, fortargeting outlet 2, the delivery efficiency was 100% for starting points of 70 mm or less, 74% at 90 mm, and 42% at 110 mm. The overall average delivery efficiency across all three outlets was 99.3% for starting points of 70 mm or less, 85.3% at 90 mm, and 63.3% at 110 mm. These results demonstrate the effectiveness of the proposed EMA system and targeting algorithm for guiding the magnetic particle in blood vessels with two branches, especially for starting points of 90 mm or less. Compared to the 2D and 3D Y-shaped phantoms, the 3D blood vessel phantom showed significantly lower efficiency. This is due to the additional branches that require more complex navigation, further reducing delivery efficiency.

V. Conclusion

In this study, we introduced the new open-type EMA system, the novel FFP generation method tailored for this system, and the targeting algorithm for steering the magnetic particle in 3D microvascular environments. To address the limitations of previous closed-type EMA systems, we designed and optimized the open-type EMA system, focusing on compatibility with imaging devices and spatial efficiency. Coil structure optimization using the CEPMA design led to a 50.19% increase in magnetic field strength and a 42.99% improvement in gradient compared to the FEMA structure. Additionally, we optimized the coil configuration for FFP generation by increasing the isotropy of the gradient field.

Then, the constraints for FFP generation were reduced from six to four, increasing the gradient strength in the desired direction while maintaining isotropy. Additionally, we developed a targeting algorithm for guiding the magnetic particle to desired locations within complex vascular structures. The various simulations and experiments performed in 2D and 3D Y-shaped phantoms, as well as in a 3D phantom modeled after liver vasculature, demonstrated that the proposed open-type EMA system and targeting algorithm effectively guide the magnetic particle to target outlets in various vascular structures. The proposed system achieved delivery efficiencies of over 96% for starting points within 70 mm, with average efficiencies of 88.3%, 82%, and 63.3% in the 2D Y-shaped, 3D Y-shaped, and liver-model 3D phantoms at 110 mm. While the algorithm showed robust single-particle control, multi-particle scenarios may introduce discrepancies due to inter-particle interactions. Future work will explore clustering effects and develop algorithms for multi-particle control. Ex-vivo and in-vivo experiments will assess clinical applicability, addressing challenges from real blood vessel properties and flow dynamics. These findings are expected to advance non-invasive targeted drug delivery systems using magnetic actuation technology.

References

[1] Y. L. Liu, D. Chen, P. Shang, and D. C. Yin, "A review of magnet systems for targeted drug delivery," *Journal of Controlled Release*, vol. 302, pp. 90–104, 2019.

[2] S. Senapati, A. K. Mahanta, S. Kumar, and P. Maiti, "Controlled drug delivery vehicles for cancer treatment and their performance," *Signal Transduction and Targeted Therapy*, vol. 3, no. 1, pp. 1, 2018.

[3] R. H. Muller and C. M. Keck, "Challenges and solutions for the delivery of biotech drugs—A review of drug nanocrystal technology and lipid nanoparticles," *Journal of Biotechnology*, vol. 113, no. 1–3, pp. 151–170, 2004.

[4] Y. Wang and D. Kohane, "External triggering and triggered targeting strategies for drug delivery," *Nature Reviews Materials*, vol. 2, no. 17020, 2017.

[5] S. M. Chowdhury, T. Lee, and J. K. Willmann, "Ultrasound-guided drug delivery in cancer," *Ultrasonography*, vol. 36, no. 3, pp. 1, 2017.

[6] S. R. Sirsi and M. A. Borden, "State-of-the-art materials for ultrasound-triggered drug delivery," *Advanced Drug Delivery Reviews*, vol. 72, pp. 3–14, 2014

[7] N. S. Forbes, "Engineering the perfect (bacterial) cancer therapy," *Nature Reviews Cancer*, vol. 10, no. 11, pp. 785–794, 2010.

[8] S. S. Lucky, K. C. Soo, and Y. Zhang, "Nanoparticles in photodynamic therapy," *Chemical Reviews*, vol. 115, no. 4, pp. 1990–2042, 2015.

[9] J. F. Lovell, T. W. B. Liu, J. Chen, and G. Zheng, "Activatable photosensitizers for imaging and therapy," *Chemical Reviews*, vol. 110, no. 5, pp. 2839–2857, 2010.

[10] M. K. Manshadi, M. Saadat, M. Mohammadi, M. Shamsi, M. Dejam, R. Kamali, and A. Sanati-Nezhad, "Delivery of magnetic micro/nanoparticles and magnetic-based drug/cargo into arterial flow for targeted therapy," *Drug Delivery*, vol. 25, no. 1, pp. 1963–1973, 2018.

[11] B. J. Nelson, I. K. Kaliakatsos, and J. J. Abbott, "Microrobots for minimally invasive medicine," *Annual Review of Biomedical Engineering*, vol. 12, no. 1, pp. 55–85, 2010.

[12] J. Li, B. Esteban-Fernandez de Avila, W. Gao, L. Zhang, and J. Wang, "Micro/nanorobots for biomedicine: Delivery, surgery, sensing, and detoxification," *Science Robotics*, vol. 2, no. 4, eaam6431, 2017.

[13] S. Sharif, K. T. Nguyen, D. Bang, J. O. Park, and E. Choi, "Optimization of field-free point position, gradient field, and ferromagnetic polymer ratio for enhanced navigation of magnetically controlled polymer-based microrobots in blood vessels," Micromachines, vol. 12, no. 4, pp. 424, 2021.

[14] M. P. Bui, T.-A. Le, and J. Yoon, "A magnetic particle imaging-based navigation platform for magnetic nanoparticles using interactive manipulation of a virtual field-free point to ensure targeted drug delivery," *IEEE Transactions on Industrial Electronics*, vol. 68, no. 12, pp. 12493–12503, 2021.

[15] N. Nothnagel, J. Rahmer, B. Gleich, A. Halkola, T. M. Buzug, and J. Borgert, "Steering of magnetic devices with a magnetic particle imaging system," *IEEE Transactions on Biomedical Engineering*, vol. 63, pp. 2286–2293, 2016.

[16] Y. Kim, M. Park, H. Lee, and J. Yoon, "Automatic navigation scheme for micro-robot using magnetic potential field through field-free point," *IEEE Access*, vol. 12, pp. 30135–30145, 2024.

[17] C. Kim, J. Kim, J. O. Park, E. Choi, and C. S. Kim, "Localization and actuation for MNPs based on magnetic field-free point: Feasibility of movable electromagnetic actuations," *Micromachines*, vol. 11, no. 11, pp. 1020, 2020.

[18] K. T. Nguyen, H. S. Lee, J. Kim, E. Choi, J. O. Park, and C. S. Kim, "A composite electro-permanent magnetic actuator for microrobot manipulation," *International Journal of Mechanical Sciences*, vol. 229, pp. 107516, 2022.

[19] A. R. Conn, K. Scheinberg, and L. N. Vicente, "Introduction to Derivative-Free Optimization," MPS-SIAM Series on Optimization, SIAM, 2009.

[20] O. T. Olufowobi and O. Olowofeso, "Interrelationship between body weight and body size parameters in chinchilla and New Zealand white rabbit genotypes in Abeokuta, Nigeria," *Journal of Biology, Agriculture and Healthcare*, vol. 5, no. 4, pp. 0–4, 2017.

[21] K. T. Nguyen, H. Kee, G. Go, S. J. Kim, E. Choi, J. O. Park, S. Park, and J. Kim, "Field-free region scanning-based magnetic microcarrier targeting in multi bifurcation vessels," *Advanced Intelligent Systems*, vol. 6, no. 5, 2024.

[22] L. Wang, L. Song, H. Sun, Y. Ji, Y. Dai, and L. Feng, "Multi-mode motion control of reconfigurable vortex-shaped microrobot swarms for targeted tumor therapy," IEEE Robotics and Automation Letters, vol. 7, no. 2, pp. 3578-3583, Apr. 2022

[23] M. Park, T. Le, A. Eizad and J. Yoon, "A Novel Shared Guidance Scheme for Intelligent Haptic Interaction Based Swarm Control of Magnetic Nanoparticles in Blood Vessels," in IEEE Access, vol. 8, pp. 106714-106725, 2020